Dynamic measurement of local displacements within curing resin-based dental composite using optical coherence elastography.

Tomlins, PH; Rahman, MW; Donnan, RS

Journal of Biomedical Optics

BiomedicalOptics.SPIEDigitalLibrary.org

Dynamic measurement of local displacements within curing resin-based dental composite using optical coherence elastography

Peter H. Tomlins
Mohammed Wahidur Rahman
Robert S. Donnan

SPIE.

Peter H. Tomlins, Mohammed Wahidur Rahman, Robert S. Donnan, "Dynamic measurement of local displacements within curing resin-based dental composite using optical coherence elastography," *J. Biomed. Opt.* **21**(4), 046001 (2016), doi: 10.1117/1.JBO.21.4.046001.

Dynamic measurement of local displacements within curing resin-based dental composite using optical coherence elastography

Peter H. Tomlins,[a,*] Mohammed Wahidur Rahman,[b] and Robert S. Donnan[b]
[a]Queen Mary University of London, Barts & The London School of Medicine & Dentistry, Turner Street, London, United Kingdom
[b]Queen Mary University of London, School of Electrical Engineering & Computer Science, Mile End Road, London, United Kingdom

Abstract. This study aimed to determine the feasibility of using optical coherence elastography to measure internal displacements during the curing phase of a light-activated, resin-based composite material. Displacement vectors were spatially mapped over time within a commercial dental composite. Measurements revealed that the orientation of cure-induced displacement vectors varied spatially in a complex manner; however, each vector showed a systematic evolution with time. Precision of individual displacements was estimated to be ~1 to 2 μm, enabling submicrometer time-varying displacements to be detected. [DOI: 10.1117/1.JBO.21.4.046001]

Keywords: optical coherence tomography; optical coherence elastography; resin-based composite; dental composite; polymerization shrinkage.

Paper 150792LR received Nov. 26, 2015; accepted for publication Feb. 18, 2016; published online Apr. 1, 2016.

1 Introduction

Light-activated, resin-based composites (RBCs) are widely used in both industry[1] and medicine.[2] In dentistry, they have largely replaced mercury-based dental.[3]

Light cure RBCs are typically composed of a monomer (i.e., bisGMA, UDMA, TEGDMA), a filler material (silica and various bioglasses), and a photoinitiator system (Camphorquinone/dimethylaminoethyl methacrylate).[1,2] Illumination of the RBC with light, corresponding to the photoinitiator absorption wavelength initiates polymerization and consequent hardening of the resin into a solid material.

Optimization of the spatial cure characteristics of RBCs has been the subject of considerable research[3–5] driven by certain shortcomings of RBCs. For example, they are well known to exhibit shrinkage during cure.[6] In dentistry, shrinkage presents a clinical and technological challenge[7] resulting in stress at the tooth-restoration interface, separation fracture[8] and secondary caries.[9] Furthermore, varying degrees of polymerization[10] are expected to result in a spatially varying elastic modulus.[11]

The dynamic development of RBC elastic modulus is of importance because it necessarily effects shrinkage stress at the tooth-restoration boundary and thus impacts upon the likelihood of failure.[12,13] However, there are currently no widely available tools to visualize and measure internal physical characteristics of RBCs in real time, throughout cure. Therefore, finite element computer modeling has been used to estimate three-dimensional distributions of shrinkage stress[14] and movements[15] within restorations although curing dynamics have not been investigated.

Experimentally, curing has previously been investigated using low-coherence interferometry (LCI) to measure the refractive index change and shrinkage of RBCs.[16] The consequent internal defects of RBC restorations have been imaged using optical coherence tomography (OCT),[17] an LCI-based imaging technique. Outside of dentistry, OCT has been used to evaluate the structure of composite materials[18,19] and applied to engineering applications.[20,21]

Optical coherence elastography (OCE)[17,21,22] uses OCT to measure spatial variations in the elastic modulus of materials.[22] Under uniaxial loading conditions, the elastic modulus $E = \sigma/\varepsilon$, where the stress $\sigma = F/A$ is defined by a force F applied over an area A, and the resulting strain $\varepsilon = \Delta l/l$ is the ratio of length change Δl to the original length l. OCT measures localized deformation in response to a known applied stress. However, for optically cured dental composite, the applied stress is spatiotemporally varying in multiple directions, thus making the direct determination of the spatial elastic modulus nontrivial. Consequently, this work has been restricted to the measurement of local deformation vectors. This is a central step in OCE, and therefore, this term is used for consistency with other literature. To the authors' knowledge, OCT/OCE has not previously been applied to measuring internal deformation within curing dental composite.

Therefore, this article sets out to determine the feasibility of using OCE to dynamically measure the internal deformations within light-cured RBCs due to polymerization shrinkage.

2 Materials and Methods

A commercial RBC was investigated (Enamel shade A2, IPS Empress Direct, Ivoclar Vivadent). Following the manufacturer's instructions, it was cured for 20 s with a dental curing lamp (Optima 10, BA International Ltd). The RBC was measured before, during, and throughout cure for a total duration of 60 s using a custom-built fiber-optic OCT system. The light source was a superluminescent light-emitting diode (SLD1325, Thorlabs Ltd) operating nominally in the 1250 to 1400 nm waveband and was detected by a custom spectrometer. The spectrometer comprised a 92 kHz line scan camera (SU1024-LDH2, Sensors Unlimited) and a reflective diffraction grating

*Address all correspondence to: Peter H. Tomlins, E-mail: p.h.tomlins@qmul.ac.uk

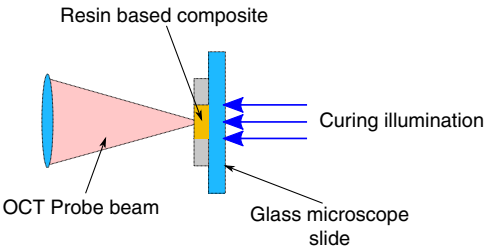

Fig. 1 Experimental configuration. The resin-based composite was constrained within a 0.75 mm deep, 4 mm diameter ring placed on a glass microscope slide through which the OCT probe beam and the curing lamp illuminated the sample.

(1200 lines per mm). The OCT point spread function (PSF) was characterized by its axial and lateral full width half maxima (FWHM) of 7.8 ± 1.0 and 9.1 ± 1.7 μm, respectively [uncertainty represents 95% confidence interval (CI)]. The experiment was configured as depicted in Fig. 1 and was repeated three times.

The RBC was placed into a circular washer (diameter = 4 mm, thickness = 0.75 mm). A glass microscope slide (nominal thickness 1 mm) provided a transparent substrate through which the specimen was illuminated with the curing lamp. The OCT system was configured to acquire B-scans at a fixed location across the central region of the specimen. A series of 100 logarithmically scaled OCT B-scan intensity images were obtained at a rate of one every 600 ms. The spectrometer integration time was 100 μs, enabling single B-scan acquisition within 50 ms, followed by a delay of 550 ms between B-scans. The total acquired B-scan image width was nominally 3 mm acquired over 500 A-scans, yielding a nominal lateral pixel size of 6.9 μm. For comparison, the axial pixel size was nominally 9.5 μm.

The OCT images were analyzed numerically using a custom MATLAB script (Mathworks). Each B-scan was divided into a grid of 84 regions of interest (ROIs), each measuring $M = 25 \times N = 25$ pixels ($\sim 173 \times 238$ μm^2) in the lateral and axial directions, respectively. The cross-correlation of each ROI, C_t, was calculated between corresponding ROIs in the first OCT image in the time series, ROI_0, and each subsequent B-scan, ROI_t, at time t using Eq. (1).

$$C_t(p,q) = \sum_{m=0}^{M-1}\sum_{n=0}^{N-1} \mathrm{ROI}_0(m,n)\mathrm{ROI}_t^*(m-p,n-q). \quad (1)$$

The local displacement vector, $\mathbf{dr} = \mathbf{R} - [p_0, q_0]^T$, at each timepoint and within each ROI was estimated by calculating the centre of mass, $\mathbf{R}$, of the cross-correlation, Eq. (2), and subtracting from it the ROI centre, $[p_0, q_0]^T$.

$$\mathbf{R} = \frac{1}{\sum_p \sum_q C_t(p,q)} \sum_p \sum_q C_t(p,q) \begin{bmatrix} p \\ q \end{bmatrix}. \quad (2)$$

For comparison with the internal displacement measurements, the bulk optical specimen thickness was estimated for each B-scan. The average specimen A-scan profile along the axial (z) dimension resembles a rectangular function of the form $\Pi(z) = 0$ if $|z| > 0.5$, 0.5 if $|z| = 0.5$, 1 if $|z| < 0.5$. A smooth approximation to the rectangular function can be constructed from the product of two error functions, Eq. (3), which is well behaved under parameter optimization.

$$\Phi(z) = A\mathrm{erf}\{\gamma[z - (z_0 - w/2)]\}\mathrm{erf}\{\gamma[(z_0 + w/2) - z]\} + k. \quad (3)$$

Parameters A, z_0, k, and w represent the maximum intensity, z-position, noise floor, and specimen thickness, respectively. A constant edge steepness parameter γ was manually determined to approximately match the A-scan signal intensity gradient at the material surface. The specimen thickness w was obtained at each time point by minimization of the sum of the squared difference between Eq. (3) and the mean A-scan intensity profile.

3 Results

The mean thickness change for all three experiments is plotted as a function of time in Fig. 2. The error bars represent the 95% CI.

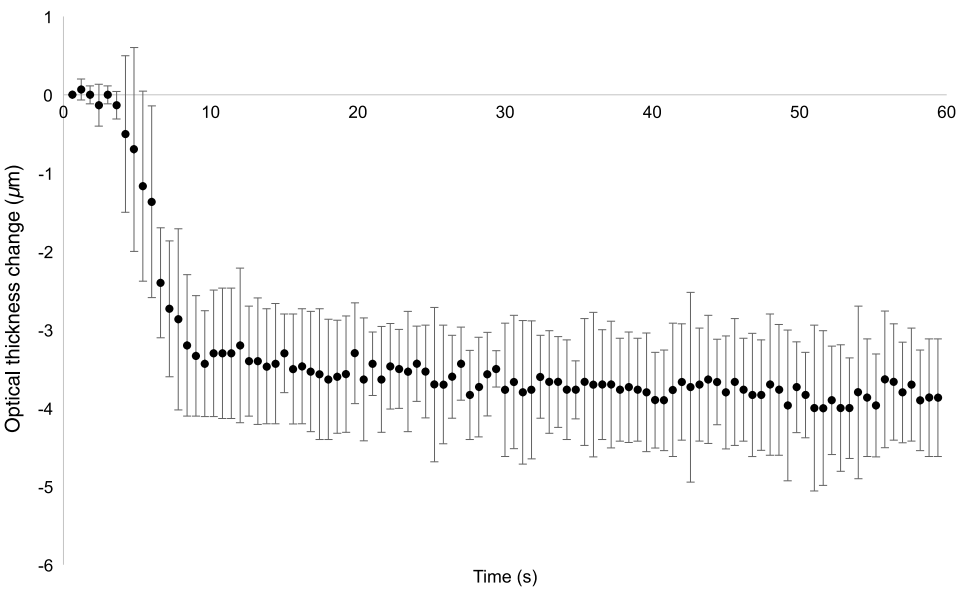

Fig. 2 Mean optical thickness change for the three dental composite specimens measured over a 60 s period. Error bars represent 95% CIs for the mean thickness change over three independent experiments.

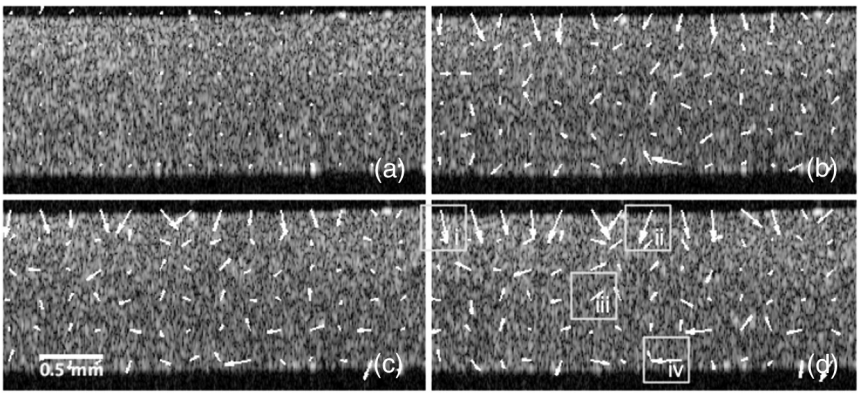

Fig. 3 Local displacement vectors showing the internal displacement of filler particles at time-points throughout the curing process. (a) Prior to illumination with the curing lamp, $t = 0.6$ s, (b) at the initiation of cure, $t = 3.6$ s, (c) $t = 5.4$ s, and (d) mid-way through the curing process, $t = 7.8$ s. Boxes i-iv in (d) indicate regions plotted in Fig. 4.

Displacement vectors were calculated at each time point for each ROI. These are shown as white arrows in Fig. 3 for time points $t = 0.6$ s, $t = 3.6$ s, $t = 5.4$ s, and $t = 7.8$ s. At a given point in time, the direction of the displacement vectors does not follow a smooth spatial distribution, but instead exhibits a complex arrangement. However, each vector was observed to systematically evolve over time both in direction and magnitude.

This systematic evolution is shown in Figs. 4(a)–4(d) for four selected displacement vectors. The specific vector locations are

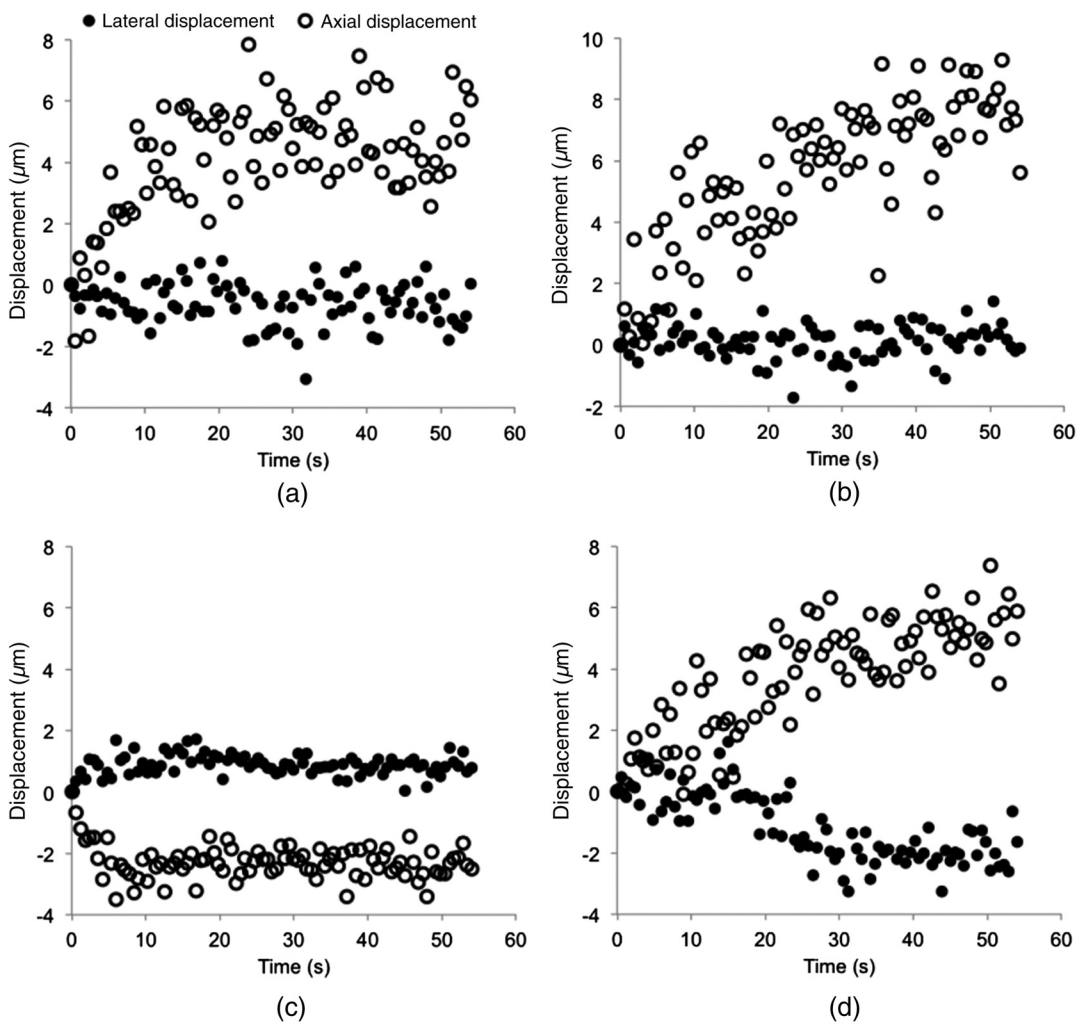

Fig. 4 Evolution of four displacement vectors (a) to (d), corresponding positions shown in Fig. 3(d) i-iv. The positive axial direction extends from the top to the bottom of the OCT B-Scan and the positive lateral direction is from left to right.

identified in Fig. 3(d) as corresponding sub-images i-iv. The top of the image represents the side farthest from the curing light from which the samples were imaged with OCT. The plots have been aligned such that $t = 0$ s represents the time at which cure was initiated. Positive axial displacement represents movement toward the curing light (bottom of the OCT image).

Figure 4(a) shows a vector in the top left of the specimen at the furthest point from the curing light. Axially, a displacement of ~6 μm is observed over the 20 s curing period. Laterally, there is no statistically discernable change, although the vectors indicate a movement toward the center. The top-center vector, represented by Fig. 4(b), exhibits similar behavior, with an axial displacement of ~8 μm observed over the entire measurement period, including postillumination. The central vector, Fig. 4(c), exhibits ~3 to 4 μm displacement away from the curing light for the first 10 s of illumination, although this appears to cease thereafter. Laterally, there is ~1 μm of movement to the right that occurs for the entire illumination period with an apparent reversal during the postillumination period. Figure 4(d) shows the displacement of a region near to the illuminated surface. An axial displacement of 6 μm was measured over the entire illumination and postillumination period. Systematic lateral displacement of 2 μm was observed postillumination. Notably, the top-center vector [Fig. 4(b)] moves toward the light (down) by ~8 to 9 μm compared to the bottom-center vector [Fig. 4(d)], which shows a displacement of 5 to 6 μm. Thus, the net displacement of the top and bottom surfaces was in the range of 3 to 4 μm, which agrees with the bulk shrinkage plot, Fig. 2, to within the 95% CI.

To characterize these results, three forms of precision were calculated in terms of the displacement standard deviation, σ. The ROI precision (σ_{ROI}) represents the repeatability of displacement measurements from a single ROI in a given specimen. Each ROI precision was estimated from all 16 displacements measured during the final 10 s of each experiment. During this time, the displacement change due to material cure was assumed to be negligible.

The mean intraspecimen precision (σ_s) is the mean of σ_{ROI} over all 84 ROIs in a single specimen. Along with its 95% CI, it estimates the repeatability of a single displacement measurement from a given specimen regardless of ROI. This provides a baseline level of measurement noise present in the analysis, although displacement sensitivity can be improved by averaging over multiple measurements. Finally, the precision reproducibility (σ_r) was assessed across all three specimens as the standard deviation of σ_s. This provides an estimate of how much the overall specimen precision varies between experiments.

The mean intraspecimen precision (σ_s) and associated 95% CI was determined over all 84 ROIs within the B-scan field of view. The resulting specimen-dependent lateral and axial displacement precisions are shown in Tables 1 and 2, respectively, for all three experiments.

Table 1 shows that the intraspecimen lateral precision was found to range between 1.06 and 1.80 μm across all the three specimens. Axially, Table 2 shows a greater spread, with a mean intraspecimen axial precision range of 1.48 to 5.16 μm. Axial precision in sample 1 was less than half that in samples 2 and 3. Similarly, sample 1 also exhibited lower lateral precision than the other samples.

Nevertheless, experimental reproducibility (σ_r) of the precision estimates was assessed from all three repetitions of the experiment. Laterally, $\sigma_r^{lat} = 0.31$ μm compared to an axial reproducibility of $\sigma_r^{axial} = 1.70$ μm. In each experiment, the lateral displacement was found to have a greater precision than the axial precision. However, over all the experiments, no statistical difference could be discerned (Mann-Whitney U Test, $p > 0.05$). This was largely due to the lower precision observed in sample 1 and the relatively low number of specimens. Notwithstanding this, there is nothing visible in the image data to suggest a problem with sample 1, and therefore, the result should be considered representative of the experimental reproducibility.

Table 1 Mean intraspecimen lateral precision (σ_s^{lat}) measured as the mean standard deviation of all displacement vectors 50 to 60 s post-cure. The CI represents 95% probability that the mean precision falls between the lower and upper bounds for each specimen.

Sample	Mean precision σ_s^{lat} (μm)	Lower 95% CI (μm)	Upper 95% CI (μm)	95% CI (μm)
1	1.71	1.62	1.80	0.09
2	1.30	1.24	1.36	0.06
3	1.11	1.06	1.16	0.05

Table 2 Mean intraexperimental axial precision (σ_s^{axial}) measured as the standard deviation of all displacement vectors at 50 to 60 s post-cure. The CI represents 95% probability that the mean precision falls between the lower and upper bounds in each experiment.

Sample	Mean precision σ_s^{axial} (μm)	Lower 95% CI (μm)	Upper 95% CI (μm)	95% CI (μm)
1	4.71	4.26	5.16	0.34
2	2.02	1.92	2.02	0.09
3	1.56	1.48	1.64	0.08

4 Discussion

Displacement precision was greater laterally compared to axially. This is because the lateral pixel spacing (6.9 μm) was $\sim(6.9\ \mu m - 9.1\ \mu m)/9.1\ \mu m = 24\%$ smaller than the lateral PSF FWHM (9.1 μm), compared to the axial pixel spacing (9.5 μm) that was $(9.5\ \mu m - 7.8\ \mu m)/7.8\ \mu m = 21\%$ larger than the corresponding axial PSF FWHM (7.8 μm). Thus, laterally, the PSF FWHM is sampled more than once due to the pixel spacing, but axially the PSF FWHM is under-sampled. This is critical because the speckle size is dependent upon the PSF. Insufficient sampling of the speckle necessarily reduces displacement precision. Lateral sampling density can be controlled experimentally, although for this work it was preferred to maximize the scan width relative to the number of A-scans permitted by the specific OCT implementation. The axial pixel spacing, Δz, in a spectral domain OCT system is proportional to the reciprocal of the detected spectral width $\Delta\nu$, i.e., $\Delta z \propto 1/\Delta\nu$. The spectrometer design can be improved to optimize axial speckle sampling, although eventually this amounts to zero-padding the spectrum and consequent sinc interpolation. Alternatively, phase sensitive algorithms can measure displacement with nanometer precision.[23,24] However,

phase-based methods are limited to measuring axial components of displacement vectors. Speckle tracking is advantageous because it has the potential to track three-dimensional deformation directly.[25] This is important for dental composites that have been shown to exhibit complex local displacement. Furthermore, phase sensitive detection requires processing of the raw interferometric data and places stringent requirements on experimental stability. In laboratory systems such as ours, phase information is readily available, although such data are not necessarily accessible in commercial OCT systems.

The precision values reported in this paper represent single-point measurements. However, for continuous time-series measurements as shown in Fig. 4, submicrometer relative displacement changes can be detected in both axial and lateral dimensions. It is these systematic and continuous changes that support the findings, that OCE can detect polymerization-borne displacements occurring within a curing composite material.

Overall, less displacement was observed laterally than axially. It is expected that bonding to the sides of the circular retaining ring resisted lateral displacement, while axially the unconstrained composite surface allowed a higher degree of deformation. At the base of the specimen, the composite becomes fixed as it adheres to the glass slide. However, away from the boundary, the composite is relatively unbound. Thus, polymerization shrinkage results in the unbound material moving toward the bound RBC. Hence, close to the interface, displacement vectors point toward the illumination lamp.

The results show that away from the glass–RBC boundary, the local displacements follow a complex spatial arrangement rather than a continuous deformation as seen in compression experiments with solid phantoms. The observed spatial arrangement of displacement vectors is similar to the turbulent flow of a viscous fluid. However, the RBC is not a homogeneous liquid, but exhibits varying degrees of monomer-polymer conversion and solid filler material. Local displacement occurs when there is a net applied stress. The source of the applied stress is polymerization shrinkage, which acts in combination with adhesion of the resin at its constrained boundaries, adhesion to filler particles, and friction generated by interacting filler particles. Computational models could be used to explore this and define the distribution of internal stress. Experimentally, polarization sensitive OCT may allow direct measurement of the shrinkage stress. The deformation results imply elastic modulus heterogeneity. However, OCT makes optical measurements with an inherent ambiguity between changes in refractive index, n, and physical deformation, d. The bulk optical thickness measurements shown in Fig. 2 therefore represent the product $w = nd$. Previous work[16] resolved this ambiguity, justifying the approximation that physical thickness change dominates for bulk material. Whether this is true for local displacements remains to be fully elucidated. Therefore, future research will focus upon understanding the relationship among optical deformation measurement, shrinkage stress, and clinical outcomes.

The results presented in this paper demonstrate the feasibility of using OCE to dynamically measure and spatially map local polymerization displacement within a light-cured composite material. A baseline level of precision and reproducibility has been estimated based upon speckle tracking from B-scan images. These results have applications in a variety of fields from clinical dentistry to aerospace engineering.

References

1. L. C. Nicolae et al., "The effect of UDMA/TEGDMA mixtures and bioglass incorporation on the mechanical and physical properties of resin and resin-based composite materials," in *Conf. Papers in Science*, Vol. 2014, p. e646143 (2014).
2. E. Asmussen and A. Peutzfeldt, "Influence of UEDMA, bisGMA and TEGDMA on selected mechanical properties of experimental resin composites," *Dent. Mater.* **14**(1), 51–56 (1998).
3. K. Fujita et al., "Effect of base monomer's refractive index on curing depth and polymerization conversion of photo-cured resin composites," *Dent. Mater. J.* **24**(3), 403–408 (2005).
4. Y. K. Lee, "Influence of scattering/absorption characteristics on the color of resin composites," *Dent. Mater.* **23**, 124–131 (2007).
5. W. M. Palin et al., "In vitro cuspal deflection and microleakage of maxillary premolars restored with novel low-shrink dental composites," *Dent. Mater.* **21**(4), 324–335 (2005).
6. E. Asmussen and A. Peutzfeldt, "Direction of shrinkage of light-curing resin composites," *Acta Odontol. Scand.* **57**(6), 310–315 (1999).
7. R. J. Y. Kim et al., "Polymerization shrinkage, modulus, and shrinkage stress related to tooth-restoration interfacial debonding in bulk-fill composites," *J. Dent.* **43**(4), 430–439 (2015).
8. L. F. J. Schneider, L. M. Cavalcante, and N. Silikas, "Shrinkage stresses generated during resin-composite applications: a review," *J. Dent. Biomech.* **2010** (2009).
9. J. L. Ferracane, "Resin composite—state of the art," *Dent. Mater.* **27**(1), 29–38 (2011).
10. A. C. Shortall, W. M. Palin, and P. Burtscher, "Refractive index mismatch and monomer reactivity influence composite curing depth," *J. Dent. Res.* **87**(1), 84–88 (2008).
11. I. Sideridou, V. Tserki, and G. Papanastasiou, "Study of water sorption, solubility and modulus of elasticity of light-cured dimethacrylate-based dental resins," *Biomaterials* **24**(4), 655–665 (2003).
12. J. L. Ferracane and T. J. Hilton, "Polymerization stress—is it clinically meaningful?," *Dent. Mater.* **32**(1), 1–10 (2016).
13. J. L. Ferracane, "Developing a more complete understanding of stresses produced in dental composites during polymerization," *Dent. Mater.* **21**(1), 36–42 (2005).
14. C. Soares et al., "Delayed photo-activation effects on mechanical properties of dual cured resin cements and finite element analysis of shrinkage stresses in teeth restored with ceramic inlays," *Oper. Dent.* (2016).
15. P. Ausiello et al., "3D-finite element analyses of cusp movements in a human upper premolar, restored with adhesive resin-based composites," *J. Biomech.* **34**(10), 1269–1277 (2001).
16. P. H. Tomlins et al., "Time-resolved simultaneous measurement of group index and physical thickness during photopolymerization of resin-based dental composite," *J. Biomed. Opt.* **12**, 014020 (2007).
17. K. Ishibashi et al., "Swept-source optical coherence tomography as a new tool to evaluate defects of resin-based composite restorations," *J. Dent.* **39**(8), 543–548 (2011).
18. J. P. Dunkers et al., "Optical coherence tomography of glass reinforced polymer composites," *Compos. A* **30**, 139–145 (1999).
19. J. P. Dunkers et al., "The prediction of permeability for an epoxy/e-glass composite using optical coherence tomography," *Polym. Compos.* **22**, 803–814 (2001).
20. P. Liu, R. M. Groves, and R. Benedictus, "Optical coherence tomography for the study of polymer and polymer matrix composites," *Strain* **50**(5), 436–443 (2014).
21. D. Stifter et al., "Investigation of polymer and polymer/fibre composite materials with optical coherence tomography," *Meas. Sci. Technol.* **19**(7), 074011 (2008).
22. B. F. Kennedy et al., "Optical coherence micro-elastography: mechanical-contrast imaging of tissue microstructure," *Biomed. Opt. Express* **5**(7), 2113–2124 (2014).
23. R. K. Wang, S. Kirkpatrick, and M. Hinds, "Phase-sensitive optical coherence elastography for mapping tissue microstrains in real time," *Appl. Phys. Lett.* **90**(16), 164105 (2007).
24. S. J. Kirkpatrick, R. K. Wang, and D. D. Duncan, "OCT-based elastography for large and small deformations," *Opt. Express* **14**(24), 11585–11597 (2006).
25. B. F. Kennedy, K. M. Kennedy, and D. D. Sampson, "A review of optical coherence elastography: fundamentals, techniques and prospects," *IEEE J. Sel. Top. Quantum Electron.* **20**(2), 272–288 (2014).